PNAS

Supporting Information for

Modular Multi-degree-of-freedom Soft Origami Robots with Reprogrammable Electrothermal Actuation

Shuang Wu, Tuo Zhao, Yong Zhu, Glaucio H. Paulino

Yong Zhu, Glaucio H. Paulino
Email: yzhu7@ncsu.edu, gpaulino@princeton.edu

This PDF file includes:

Supporting text
Figures S1 to S8
Tables S1 to S3
SI References

Other supporting materials for this manuscript include the following:

Movies S1 to S5

Supporting Information Text

1. Kresling origami geometry and design.

The cylindrical Kresling origami has two kinematic stable configurations, i.e., deployed state and folded state. These two configurations can be determined by four independent geometry parameters, i.e., the height H_1 of the unit in the deployed state, the height H_0 in the folded state, number n of polygon edges and corresponding edge lengths, b (see illustrations in Fig. S1). Based on H_1, H_0, n, and b, we compute two more geometry parameters, those are the relative twisting angles ψ_1 and ψ_0 between the top polygon and the bottom polygon in the two states, respectively (1),

$$\psi_1 = 2\tan^{-1}x_1, \quad \psi_0 = 2\tan^{-1}x_0 \tag{S1}$$

where x_1 and x_0 are defined as follows:

$$x_1 = \frac{2\,y\sin(\pi/n)}{1+\cos(2\pi/n)+z} \quad x_0 = \frac{2\,y\sin(\pi/n)}{1+\cos(2\pi/n)-z} \tag{S2}$$

and we define $y = \sin(\pi/n)\sqrt{\cot^2(\pi/n)\csc^2(\pi/n) - [(H/b)^2 - (H_0/b)^2]^2} - \cos(\pi/n)$ and $z = [1-\cos(2\pi/n)][(H/b)^2 - (H_0/b)^2]$.

In summary, all six geometry parameters, H_1, H_0, n, b, ψ_1, and ψ_0, fully construct the 3D configurations of the Kresling origami. Moreover, we compute design parameters of the 2D crease pattern, panel length a and angle γ, as illustrated in Fig. S1

$$a = b\sqrt{\left(\frac{H_0}{b}\right)^2 + \frac{x_0^2\csc^2(\pi/n)}{x_0^2+1}} \tag{S3}$$

$$\gamma = \cos^{-1}\left(\frac{x_0[x_0 - \cot(\pi/n)]}{\sqrt{(x_0^2+1)[(H_0/b)^2(x_0^2+1) + x_0^2\csc^2(\pi/n)]}}\right) \tag{S4}$$

In the Results section, the Kesling robot segment has the following parameters, i.e., H_1 = 20.9 mm, H_0 = 6.3 mm, n = 8, b = 13.9 mm, $\psi_1 = 48.3°$, $\psi_0 = 86.7°$, a = 25.3 mm, and $\gamma = 113°$.

2. Reduced-order modeling for Kresling robot segments.

Modeling details. The schematic diagram of the reduced order model used for simulating a Kresling unit is shown in Fig. S8(A). The total elastic energy, U, is the sum of the elastic energy stored in the stretching bars, U_{bar}, and that provided by the rotational springs, U_{spr}. The total energy can be calculated as:

$$U = U_{bar} + U_{spr} = \frac{1}{2}k_s\left(n_m\delta_m{}^2 + n_v\delta_v{}^2 + n_b\delta_b{}^2\right) + \frac{1}{2}k_r N_r \Delta_\beta{}^2 \tag{S5}$$

where subscripts m, v, b denote the stretching bars along the mountain creases, valley creases, and octagon edges, respectively. The parameters n, L, δ denote number of the bars, lengths of the bars in the undeformed configuration, and length changes of the bars, respectively. Moreover, N_r is the number of the rotational springs, and Δ_β is the change of the dihedral angle related to the springs. Finally, the stiffness of the stretching bar is defined as $k_s = \overline{k_s}/L$ (where $\overline{k_s}$, measured by (N mm^{-1})mm, denotes the normalized stretching stiffness), and the stiffness of the rotational spring is defined as $k_r = \overline{k_r}L$ (where $\overline{k_r}$, measured by N mm(rad mm)$^{-1}$, denotes rotational stiffness of the fold line per unit length). Given a constant $\overline{k_s}$, e.g., $\overline{k_s} = 80$ (N mm^{-1})mm, we vary $\overline{k_r}$ from 0 to 4×10^{-2} N mm(rad mm)$^{-1}$, and illustrate how the stiffness ($\overline{k_r}$) influence the monostable and bistable behaviors (Fig. S8B). For $\overline{k_r} = 0$, the origami unit has two zero-energy kinematically stable configurations. In this case, panel stretching dominates the deformation. As $\overline{k_r}$ increases, the position of the second stable state changes. This is due to the monotonically increasing energy contributed by panel folding. For $\overline{k_r} = 4 \times 10^{-2}$ N mm(rad mm)$^{-1}$, the origami unit behaves monostably.

Nonlinear solution scheme. We present an incremental-iterative approach to solve the nonlinear equilibrium equation [3] in the main text, i.e., $T(u) = \chi(u)f$. At each incremental step, a series of iterations is conducted until convergence is achieved. The present incremental-iterative scheme is given by

$$K_{j-1}^k \delta u_j^k = \delta \chi_j^k f + r_{j-1}^k \qquad \text{[S6]}$$

where the superscript k and the subscript j denote the present increment and the iteration, respectively, the item K_{j-1}^k denotes the tangent stiffness matrix at the previous $j - 1$ iteration. We define the residual vector at the previous $j - 1$ iteration as $r_{j-1}^k = \chi_{j-1}^k f - T(u_{j-1}^k)$, and calculate the displacements and load factor by adding contributions from previous iterations, such as:

$$u_j^k = u_{j-1}^k + \delta u_j^k \qquad \text{[S7]}$$

$$\chi_j^k = \chi_{j-1}^k + \delta \chi_j^k \qquad \text{[S8]}$$

The augmented system in Eq. [S6] has (N + 1) unknowns, i.e., N displacement components (δu_j^k) and one load parameter $(\delta \chi_j^k)$, but only N equations. Therefore, we add an additional constraint equation as follows to compute the load factor:

$$a_j^k \cdot \delta u_j^k + b_j^k \delta \chi_j^k = c_j^k \qquad \text{[S9]}$$

where the vector of unknowns (δu_j^k) can be decomposed into two parts

$$\delta u_j^k = \delta \chi_j^k \delta u_{f_j}^k + \delta u_{r_j}^k \qquad \text{[S10]}$$

such that Eq. [S6] becomes

$$\begin{aligned} K_{j-1}^k \delta u_{f_j}^k &= f \\ K_{j-1}^k \delta u_{r_j}^k &= r_{j-1}^k \end{aligned} \qquad \text{[S11]}$$

Solving Eq. [S9] for $\delta \chi_j^k$ and combining it with Eq. [S10] yields the new constraint expression as

$$\delta \chi_j^k = \frac{c_j^k - a_j^k \cdot \delta u_{r_j}^k}{a_j^k \cdot \delta u_{f_j}^k + b_j^k} \qquad \text{[S12]}$$

where the constraint parameters, a_j^k, b_j^k, c_j^k are defined by the selected nonlinear solution scheme. In this work, we use the Modified Generalized Displacement Control Method (MGDCM) (2), a variant of the arc-length method, as the solution scheme. The associated constraint parameters are specified as

$$a_j^k = \delta \chi_1^k \delta u_{f_1}^k, \quad b_j^k = 0 \qquad \text{[S13]}$$

and

$$c_j^k = \begin{cases} c & \text{for } j = 1 \\ 0 & \text{for } j \geq 2 \end{cases} \qquad \text{[S14]}$$

where c is defined as:

$$c = (\delta \chi_1^1)^2 \delta u_{f_1}^1 \cdot \delta u_{f_1}^1 \qquad \text{[S15]}$$

and $\delta \chi_1^1 = \overline{\delta \chi}$ is the prescribed initial load factor at the first iteration of the first increment (i.e., $k = j = 1$). Since $\delta u_{r_1}^k = 0$, the load factor in Eq. [S12] when $j = 1$ and $k \geq 2$ becomes

$$\delta \chi_1^k = \frac{\overline{\delta \chi}^2 \delta u_{f_1}^1 \cdot \delta u_{f_1}^1}{\delta \chi_1^k \delta u_{f_1}^k \cdot \delta u_{f_1}^k} = \pm \overline{\delta \chi} \left| \frac{\delta u_{f_1}^1 \cdot \delta u_{f_1}^1}{\delta u_{f_1}^k \cdot \delta u_{f_1}^k} \right|^{1/2} \qquad \text{[S16]}$$

3

The sign of $\delta\chi_1^k$ in Eq. [S16] is determined by the sign of the inner product $\left(\delta\boldsymbol{u}_{f_1}^{k-1} \cdot \delta\boldsymbol{u}_{f_1}^k\right)$, which will change only when the equilibrium configuration contains a load limit point. This fact implies that the sign of $\delta\chi_1^k$ corresponds to the sign of the stiffness of the system. In summary, the load factor increment $\delta\chi_j^k$ in the jth iteration of the kth increment is determined by

$$\delta\chi_j^k = \begin{cases} \overline{\delta\chi}, & k=1, j=1; \\[2mm] -\dfrac{\delta\boldsymbol{u}_{f_1}^1 \cdot \delta\boldsymbol{u}_{f_j}^1}{\delta\boldsymbol{u}_{f_1}^1 \cdot \delta\boldsymbol{u}_{f_j}^1}, & k=1, j\geq 2; \\[3mm] \pm\overline{\delta\chi}\left|\dfrac{\delta\boldsymbol{u}_{f_1}^1 \cdot \delta\boldsymbol{u}_{f_1}^1}{\delta\boldsymbol{u}_{f_1}^k \cdot \delta\boldsymbol{u}_{f_1}^k}\right|^{1/2}, & k\geq 2, j=1; \\[3mm] -\dfrac{\delta\boldsymbol{u}_{f_1}^k \cdot \delta\boldsymbol{u}_{f_j}^k}{\delta\boldsymbol{u}_{f_1}^k \cdot \delta\boldsymbol{u}_{f_j}^k}, & k\geq 2, \quad \geq 2. \end{cases} \tag{S17}$$

Note that the choice of the initial load factor $\overline{\delta\chi}$ can have a major influence on the arc-length method, and generally, a small value is chosen to capture complex nonlinear behaviors. Even so, the method can yield poor or non-convergent results for slightly larger values of the load factor. However, the adopted MGDCM is not very sensitive to the value of the initial load factor, and we can get converged results for a relatively wide range of $\overline{\delta\chi}$. The algorithm in Table S3, including a pseudo-code, summarizes the aforementioned incremental-iterative scheme.

3. Bending performance of the bimorph actuator.

The local curvature of the bimorph actuator can be calculated with Timoshenko's expression:

$$k = \frac{6(\alpha_1 - \alpha_2)(T - T_0)(1 + m)^2}{h\left[3(1 + m)^2 + (1 + mn)(m^2 + \frac{1}{mn})\right]} \tag{S18}$$

where $m = t_1/t_2$ with t_1 and t_2 as the thicknesses of the two layers (PI layer and LCE layer, respectively), $h = t_1 + t_2$, $n = E_1/E_2$ with E_1 and E_2 as Young's moduli of the two layers, T_0 is the initial temperature, T is the temperature of the actuator, and α_1 and α_2 are CTEs of the two layers, respectively. The Young's modulus of PI is taken from Nexon data sheet and the Young's modulus of LCE is taken from (3). CTE of PI is 3×10^{-5} °C^{-1} (from the data sheet of Nexon), and CTE of LCE is -2.24×10^{-3} °C^{-1} (derived from the measured strain/temperature relationship of fabricated LCE ribbon).

4. Chirality of the units in the crawling robot.

In the 7-unit crawling robot, we adopt a symmetric design of chirality to achieve a robust crawling mechanism during the bidirectional locomotion. If we denote the first passive unit as "L" in chirality and "R" for the opposite, the soft robot is in the sequence of LRRLRRL. The reason for not adopting units with the same chirality (LLLLLLL or RRRRRRR) is to prevent the rolling motion. Assembling units with alternating chirality helps with stability during movement. However, fully alternating designs like LRLRLRL or RLRLRLR end up with active units in the combination of RRR or LLL, which is also not ideal for canceling the relative rotation. As a result, the design of LRRLRRL or RLLRLLR makes the whole robot symmetric and the active units in alternating chirality (RLR or LRL).
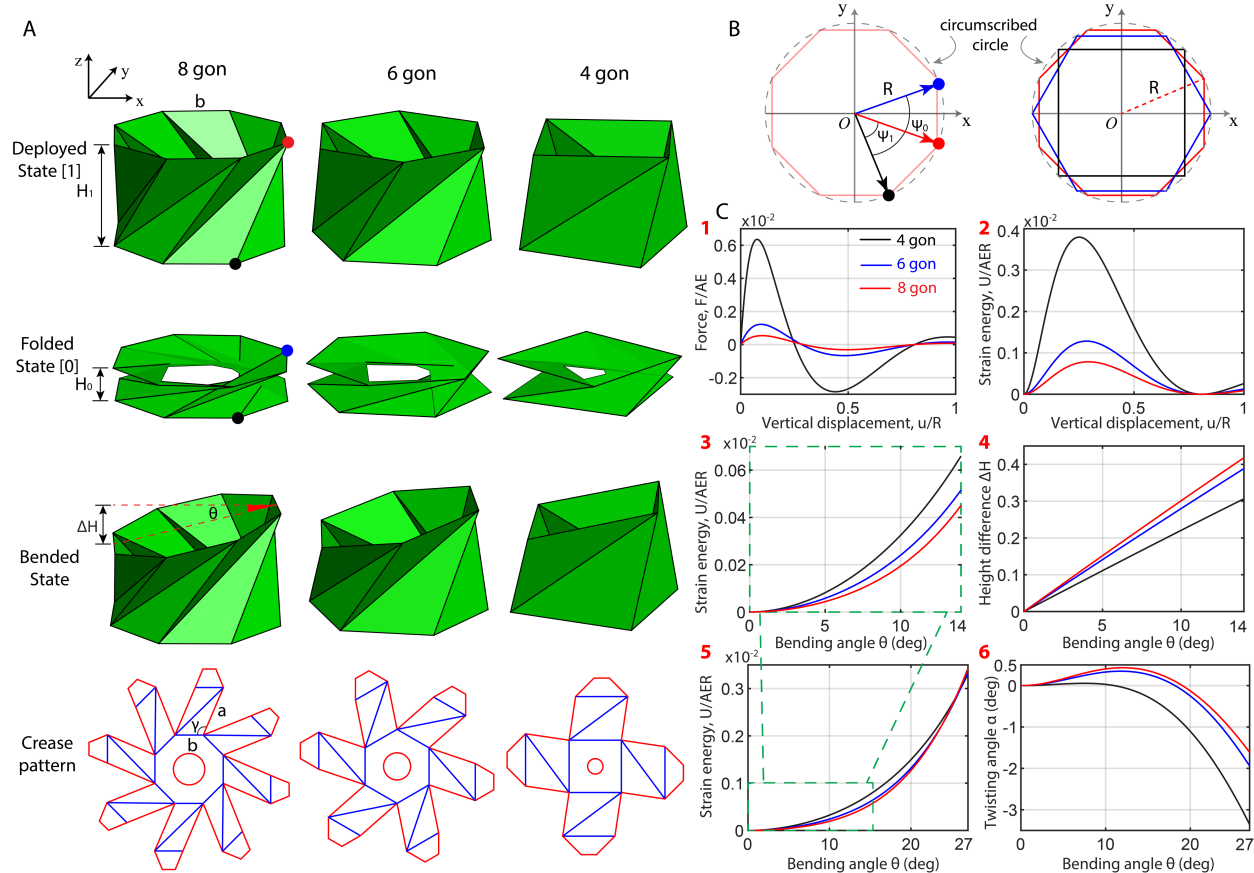
4

Fig. S1. Kresling origami design. (**A**) Three origami designs consisting of octagon, hexagon, and square shapes on top and bottom planes. Illustration of the Kresling units in three deformed configurations, i.e., deployed (first row), folded (second row), and bended (third row), respectively. The fourth row shows the origami crease patterns. All geometric parameters are listed in Table S2. (**B**) Top view of the units in the deployed state. (**C**) 1: Force applied on the top plane of the origami unit versus vertical displacement of any vertices on the top plane. 2: Stored strain energy of the unit versus vertical displacement. 3: Strain energy versus bending angle (zoom-in view of 5). 4: Height difference between the two opposite edges on the top plane versus bending angle. 5: Strain energy versus bending angle. 6: Twisting angle of the top plane versus bending angle.
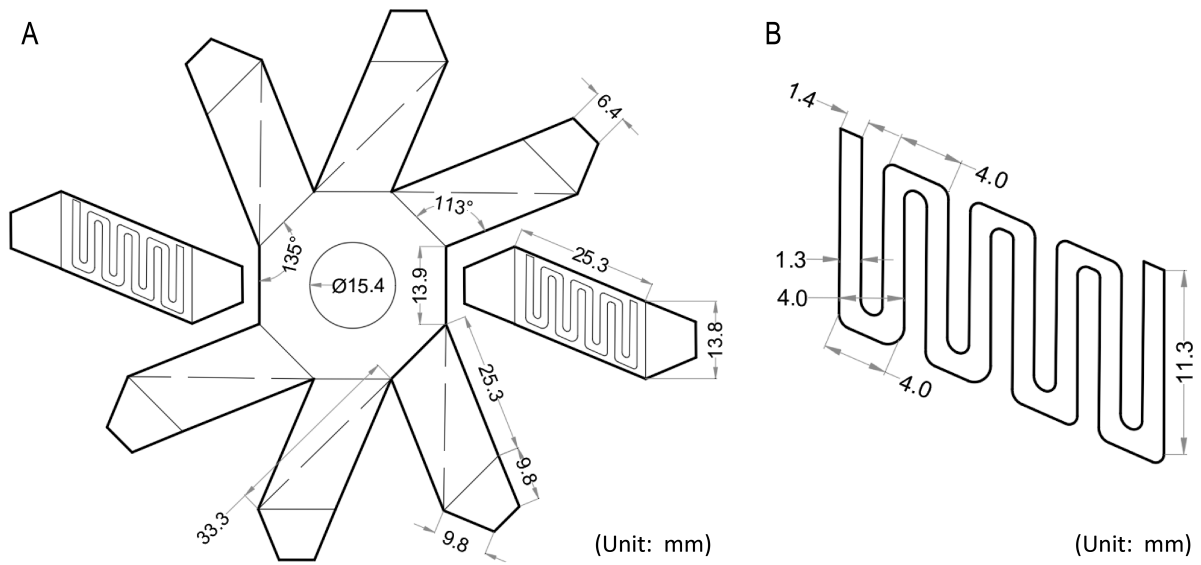
A

135°
113°
Ø15.4
13.9
6.4
25.3
13.8
25.3
9.8
33.3
9.8

(Unit: mm)

B

1.4
4.0
1.3
4.0
4.0
11.3

(Unit: mm)

Fig. S2. (**A**) Kresling pattern design with dimensions labeled (Unit: mm). (**B**) AgNW heater design with dimensions labeled (Unit: mm).
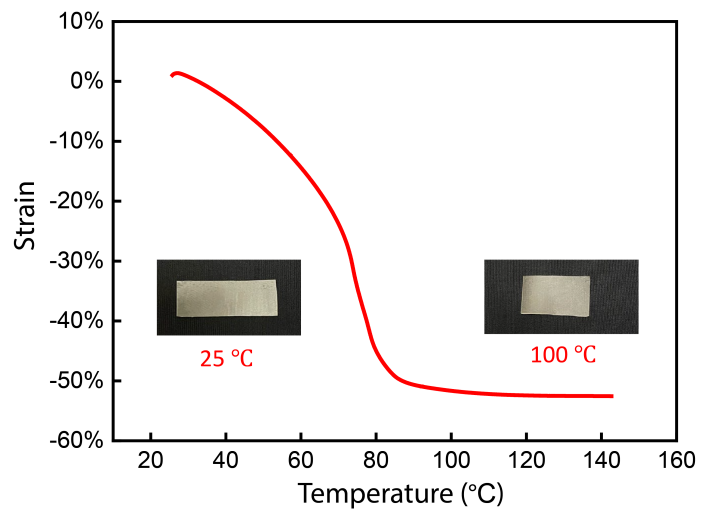
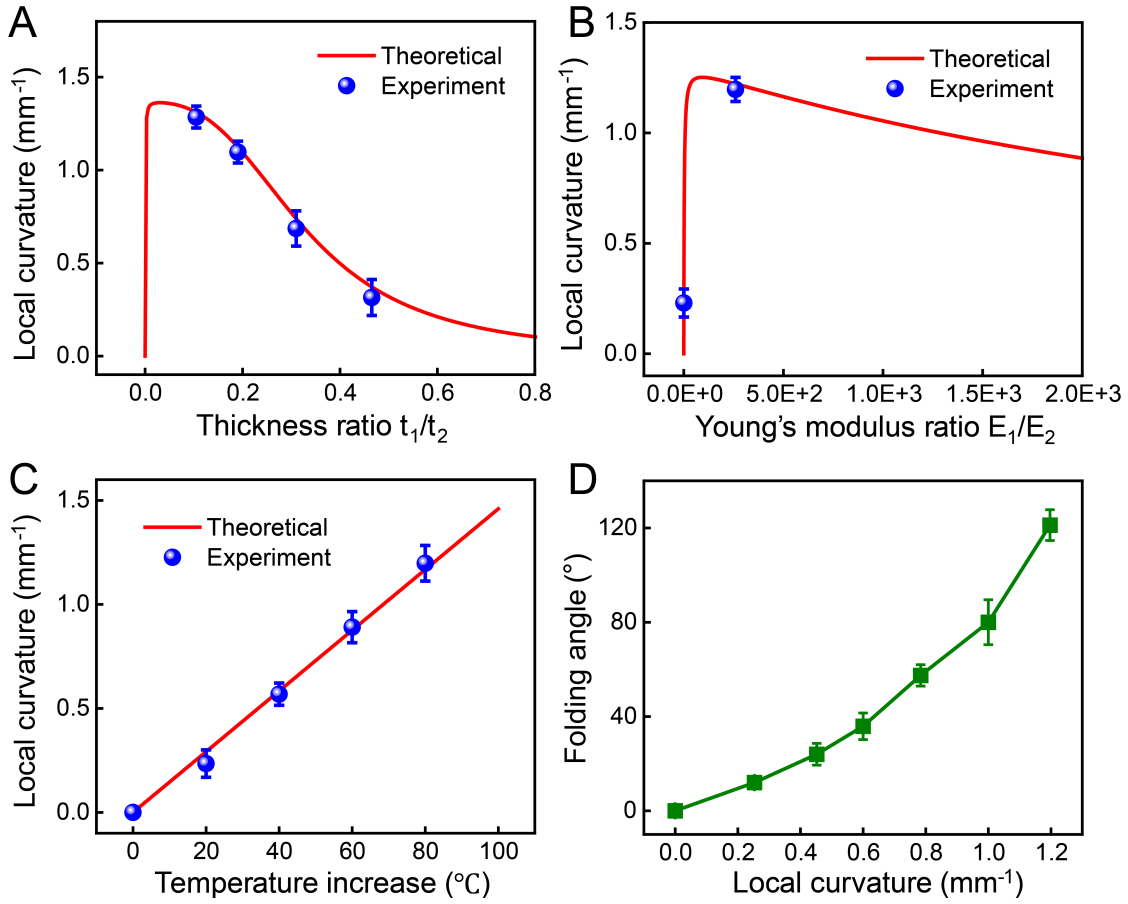**Fig. S3.** Strain/temperature relationship of the synthesized LCE film.

Fig. S4. Theoretical prediction of the bimorph bending performance of the AgNW soft actuator. Theoretical and experimental maximum curvature with respect to (**A**) thickness ratio t_1/t_2; (**B**) Young's modulus ratio E_1/E_2; and (**C**) temperature increase. (**D**) Experimental relationship between the folding angle and the local curvature at the crease line.
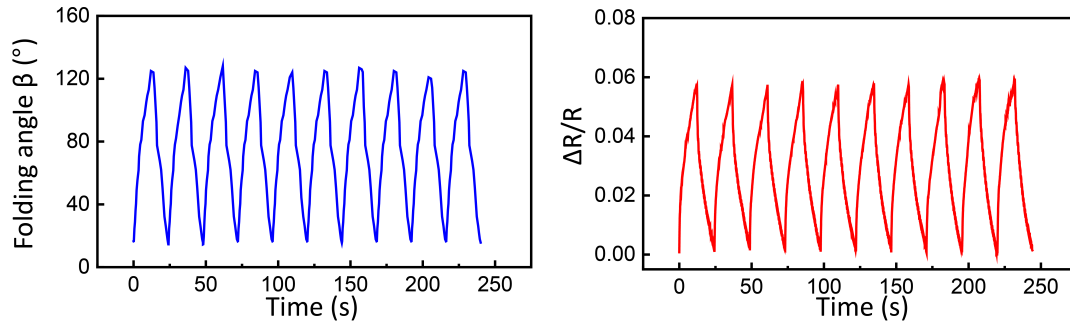
Fig. S5. The folding angle and corresponding resistance change of the AgNW heater (with 10 on/off cycles of 0.125 A).
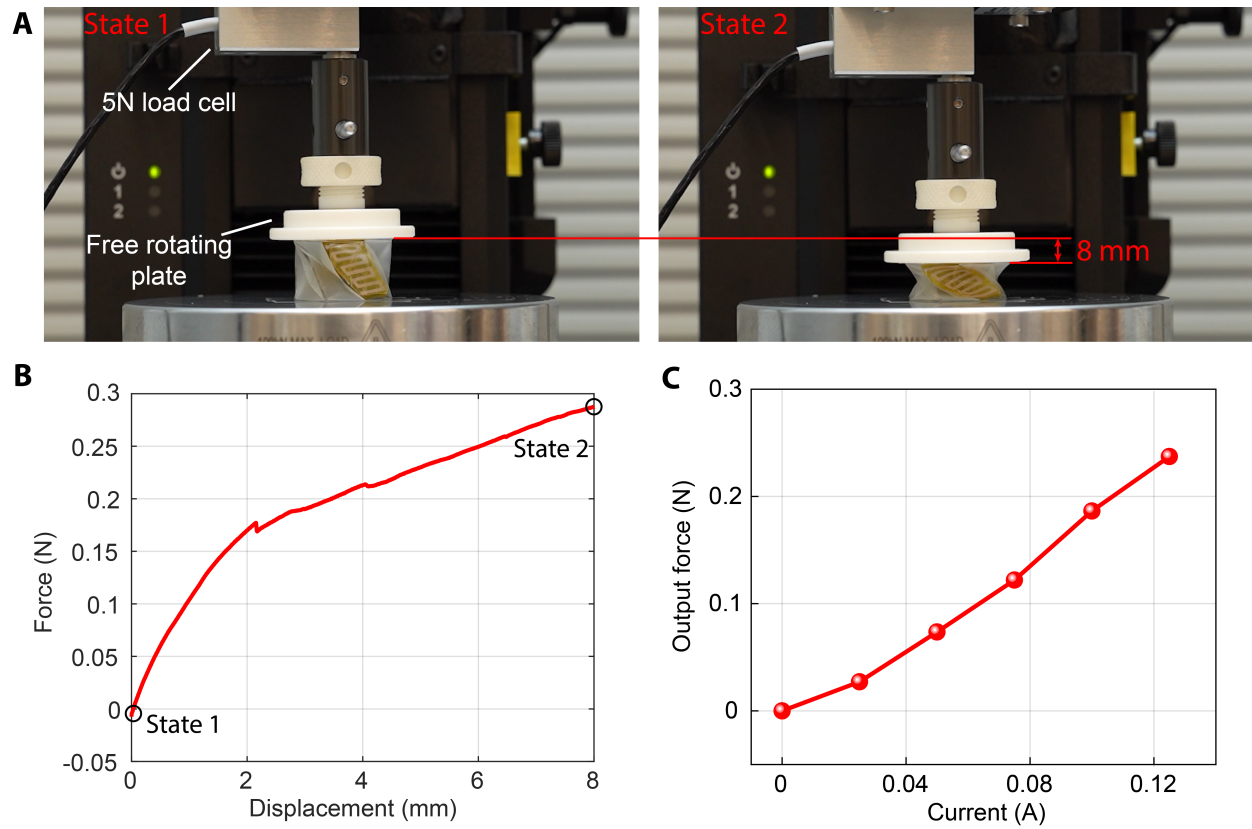
Fig. S6 (**A**) Mechanical testing setup for measuring the force-displacement relationship of a Kresling unit (two opposing side panels replaced with soft actuators). (**B**) Relationship between force and displacement. (**C**) Relationship between output force and applied current. The output force is derived from (B) and the relationship between the unit height change and applied current, provided in Fig. 3G.
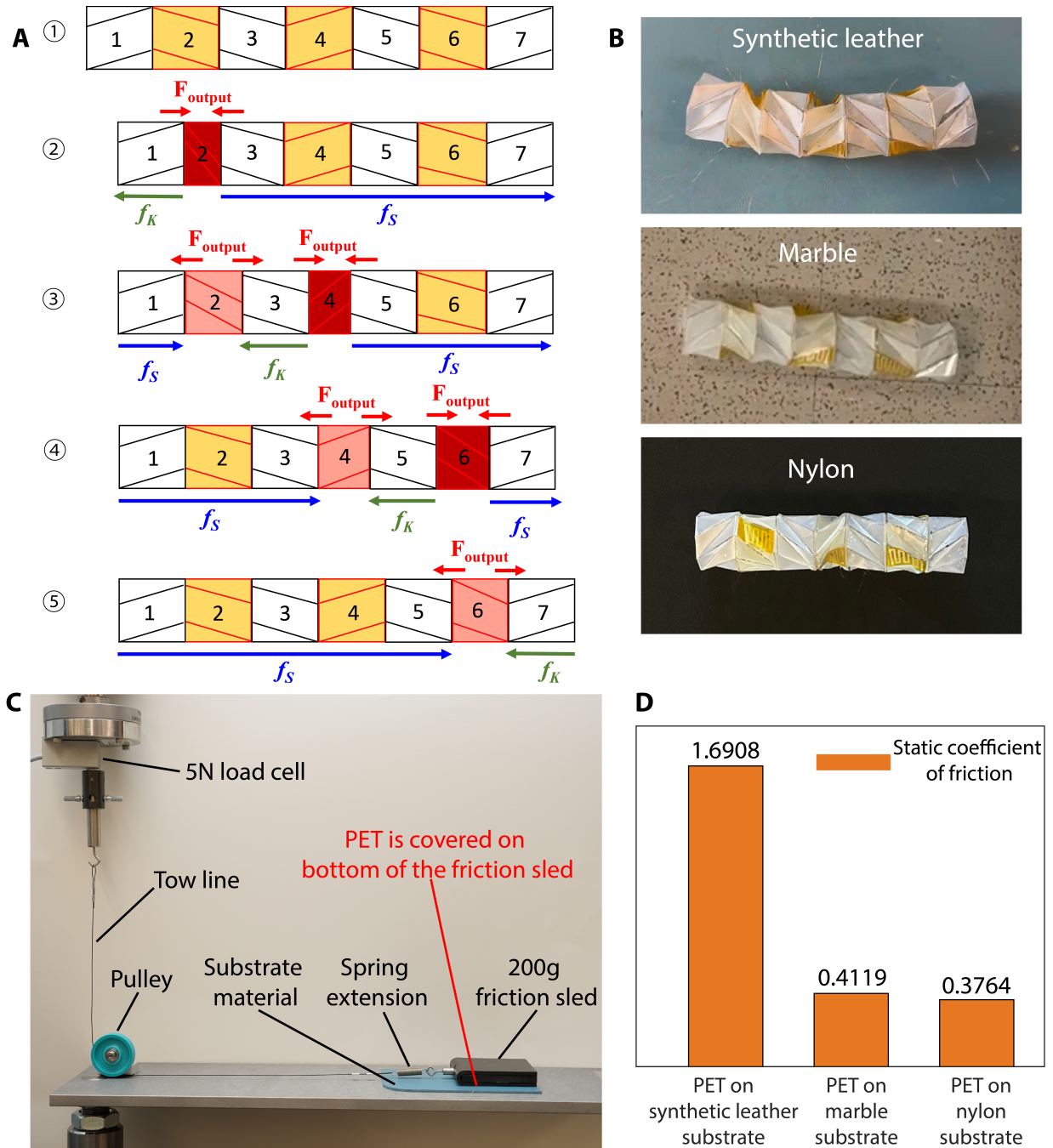
Fig. S7 (**A**) Schematics of the soft robot in one cycle of forward motion. (White: passive units; Yellow: active units. Pink: active units deploying; Red: active units folding) (**B**) Snapshots of the Kresling robot on various surfaces (synthetic leather, marble, and nylon). (**C**) Experimental setup for measuring the static coefficient of friction. (**D**) The coefficient of friction between PET (the material used for constructing the Kresling robot) and synthetic leather, marble, and nylon.
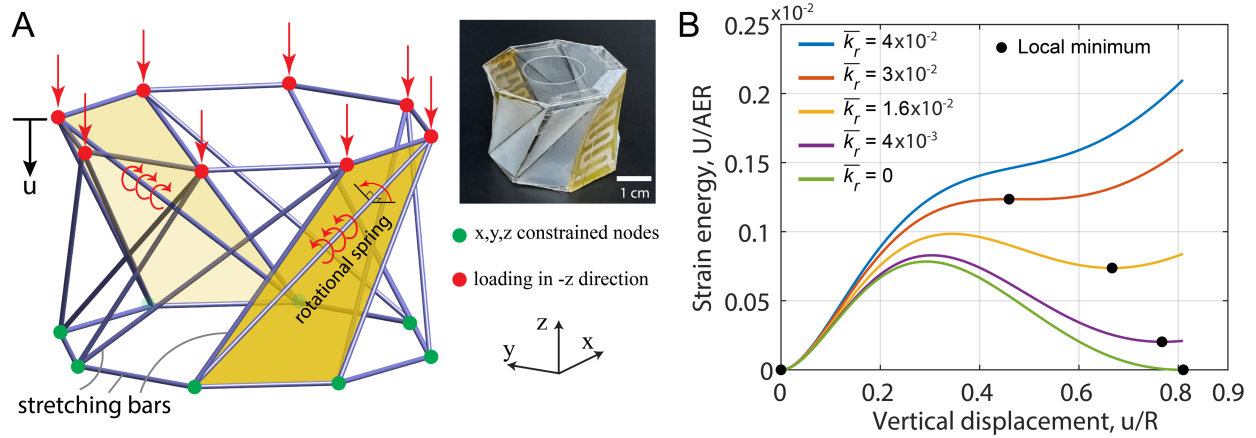
Fig. S8. Reduced-order modeling for a Kresling unit. (**A**) Schematic of the reduced order model involving both boundary conditions and loading conditions. (**B**) The stored strain energy of the Kresling unit versus the vertical displacement of any vertices on the top octagon plane. The strain energy (U/AER) and the displacement (u/R) are normalized (where E represents the material Young's modulus, A is the cross-section area of the bars, and R denotes the circumradius of the octagon). Multiple colored lines represent the solution considering a range of stiffness $\overline{k_r}$ from 0 to 4×10^{-2} N mm(rad mm)$^{-1}$. The black dot denotes the position of the stable states.

Table S1. Comparison between this work and reported soft locomotive robots.

SI Ref.	Actuation Mechanism	Locomotion Type	Locomotion modes	Actuation time (s)	Locomotion Speed
(4)	Pneumatic	Multi-gait legged	Forward	/	6.67 mm/s 0.053 body lengths per second (BL/s)
(5)	Pneumatic	Kirigami-skin	Forward	/	~3.36 mm/s ~0.0205 BL/s
(6)	Humidity	Inching	Forward	0.3	0.575 mm/s
(7)	Humidity	Inching	Forward	2	6 mm/s 0.24 BL/s
(8)	Dielectric	Inching	Forward	0.1	1.03 BL/s
(9)	Dielectric	Inching	Forward + Backward	/	7.8 mm/s 0.137 BL/s
(10)	Magnetic	Inching	Forward + Backward	0.9	34 mm/s 0.56 BL/s
(11)	Magnetic	Inching	Forward + Steering	0.2	13.2 mm/s
(12)	Magnetic	Multi-gait legged	Forward + Backward + Rigid-body Steering	0.035	~12 mm/s
(13)	Photothermal	Crawling (Peristaltic)	Forward + Backward	1.67	0.24 mm/s 0.0162 BL/s
(14)	Photothermal	Inching	Forward + Steering	/	0.33 mm/s 0.067 BL/s
(3)	Electrothermal	Inching	Forward + Backward	12	0.72 mm/s 0.012 BL/s
This work	Electrothermal	Crawling (Peristaltic)	Forward + Backward + Continuous Steering	11	0.195 mm/s 0.00476 BL/s

Table S2. Geometry parameters of the Kresling origami units.

n	H_1 (mm)	H_0 (mm)	b (mm)	ψ_1	ψ_0	a (in)	γ
8	20.9	6.3	13.9	48.3°	86.7°	25.3	113°
6	20.9	6.3	18	39.4°	80.6°	24.1	109°
4	20.9	6.3	25.4	19.5°	70.5°	21.6	99°

Table S3. Pseudo-code of the nonlinear solution scheme

Algorithm Incremental-iterative nonlinear solution scheme.

1: Set $\boldsymbol{u}_0^1 \leftarrow 0$, $\chi_0^1 \leftarrow 0$, $u^{p,1} \leftarrow 0$, $k \leftarrow 0$ for Initialization.

2: **while** $u^{p,\,k} < u^p$ **do**

3: $k \leftarrow k+1$, $j \leftarrow 0$

4: **while** $\left\|\delta \boldsymbol{u}_j^k\right\| > tol$ **do**

5:   $j \leftarrow j+1$

6:   Compute internal forces, stiffness matrix: $\boldsymbol{T}_{j-1}^k \leftarrow \boldsymbol{T}\big(\boldsymbol{u}_{j-1}^k\big)$, $\boldsymbol{K}_{j-1}^k \leftarrow \boldsymbol{K}\big(\boldsymbol{u}_{j-1}^k\big)$

7:   Compute residual vector: $\boldsymbol{r}_{j-1}^k \leftarrow \chi_{j-1}^k \boldsymbol{f}_0 - \boldsymbol{T}_{j-1}^k$

8:   Solve $\boldsymbol{K}_{j-1}^k \delta \boldsymbol{u}_{\boldsymbol{f}_0}{}_j^{\,k} = \boldsymbol{f}_0$, and $\boldsymbol{K}_{j-1}^k \delta \boldsymbol{u}_{\boldsymbol{r}}{}_j^{\,k} = \boldsymbol{r}_{j-1}^k$

9:   Determine $\delta \chi_j^k$

10:   $\delta \boldsymbol{u}_j^k \leftarrow \delta \chi_j^k \delta \boldsymbol{u}_{\boldsymbol{f}_0}{}_j^{\,k} + \delta \boldsymbol{u}_{\boldsymbol{r}}{}_j^{\,k}$

11:   Obtain iterative updates: $\boldsymbol{u}_j^k \leftarrow \boldsymbol{u}_{j-1}^k + \delta \boldsymbol{u}_j^k$, $\chi_j^k \leftarrow \chi_{j-1}^k + \delta \chi_j^k$

12: end while

13: $u^{p,\,k} \leftarrow \boldsymbol{f}_0^{\,T} \boldsymbol{u}_j^k$

14: **end while**

Movie S1. Kresling Origami Unit: folding/unfolding and controlled bending. Axial folding and unfolding of the Kresling origami unit with 6.25 V on both integrated actuators; controlled bending of the Kresling origami unit with 6.25 V on one actuator and 0 V on the other actuator.

Movie S2. Forward and backward locomotion of the Kresling soft robot by programmed actuation.

Movie S3. 8 cycles of the Kresling soft robot in steering motion by programmed actuation.

Movie S4. The Kresling soft robot following an S-shaped trajectory by programmed actuation.

Movie S5. Demonstration of an APA module picking up cargo, assembling with a PAP module, and enabling steering functionality.

SI references

1. R.J. Lang, Twists, tilings, and tessellations: mathematical methods for geometric origami, (CRC press, 2017).
2. S.E. Leon, G.H. Paulino, A. Pereira, I.F.M. Menezes, E.N. Lages, A Unified Library of Nonlinear Solution Schemes. Appl. Mech. Rev. 64, 040803 (2012).
3. S. Wu, Y. Hong, Y. Zhao, J. Yin, Y. Zhu, Caterpillar-inspired soft crawling robot with distributed programmable thermal actuation. *Sci. Adv.* **9**, eadf8014 (2023).
4. R.F. Shepherd *et al.*, Multigait soft robot. *Proc. Natl. Acad. Sci. U.S.A* **108**, 20400-20403 (2011).
5. A. Rafsanjani, Y. Zhang, B. Liu, S.M. Rubinstein, K. Bertoldi, Kirigami skins make a simple soft actuator crawl. *Sci. Robot.* **3**, eaar7555 (2018).
6. Y. He *et al.*, A highly sensitive, reversible, and bidirectional humidity actuator by calcium carbonate ionic oligomers incorporated poly (vinylidene fluoride). *Adv. Funct. Mater.* **31**, 2101291 (2021).
7. B. Shin *et al.*, Hygrobot: A self-locomotive ratcheted actuator powered by environmental humidity. *Sci. Robot.* **3**, eaar2629 (2018).
8. M. Duduta, D. R. Clarke, R. J. Wood, in 2017 IEEE International Conference on Robotics andAutomation (ICRA). (IEEE, Singapore, 2017), pp. 4346-4351.
9. Y. Xiao *et al.*, Anisotropic electroactive elastomer for highly maneuverable soft robotics. *Nanoscale* **12**, 7514-7521 (2020).
10. S. Wu *et al.*, Symmetry-breaking actuation mechanism for soft robotics and active metamaterials. *ACS Appl. Mater. Interfaces* **11**, 41649-41658 (2019).
11. Q. Ze *et al.*, Soft robotic origami crawler. *Sci. Adv.* **8**, eabm7834 (2022).
12. T. Xu, J. Zhang, M. Salehizadeh, O. Onaizah, E. Diller, Millimeter-scale flexible robots with programmable three-dimensional magnetization and motions. *Sci. Robot.* **4**, eaav4494 (2019).
13. M. Rogóż, H. Zeng, C. Xuan, D.S. Wiersma, P. Wasylczyk, Light-driven soft robot mimics caterpillar locomotion in natural scale. *Adv. Opt. Mater.* **4**, 1689-1694 (2016).
14. F. Ge, R. Yang, X. Tong, F. Camerel, Y. Zhao, A multifunctional dye-doped liquid crystal polymer actuator: light-guided transportation, turning in locomotion, and autonomous motion. *Angew. Chem.* **130**, 11932-11937 (2018).